'Sawfish' Photonic Crystal Cavity for Near-Unity Emitter-to-Fiber Interfacing in Quantum Network Applications

Julian M. Bopp, Matthias Plock, Tim Turan, Gregor Pieplow, Sven Burger, and Tim Schröder*

Photon loss is one of the key challenges to overcome in complex photonic quantum applications. Photon collection efficiencies directly impact the amount of resources required for measurement-based quantum computation and communication networks. Promising resources include solid-state quantum light sources. However, efficiently coupling light from a single quantum emitter to a guided mode remains demanding. In this work, photon losses are eliminated by maximizing coupling efficiencies in an emitter-to-fiber interface. A waveguide-integrated 'Sawfish' photonic crystal cavity is developed and finite element (FEM) simulations are employed to demonstrate that such an emitter-to-fiber interface transfers, with 97.4 % efficiency, the zero-phonon line (ZPL) emission of a negatively-charged tin vacancy center in diamond (SnV⁻) adiabatically to a single-mode fiber. A surrogate model trained by machine learning provides quantitative estimates of sensitivities to fabrication tolerances. The corrugation-based Sawfish design proves robust under state-of-the-art nanofabrication parameters, maintaining an emitter-to-fiber coupling efficiency of 88.6 %. Applying the Sawfish cavity to a recent one-way quantum repeater protocol substantiates its potential in reducing resource requirements in quantum communication.

J. M. Bopp, T. Turan, G. Pieplow, T. Schröder
Humboldt-Universität zu Berlin
Department of Physics
12489 Berlin, Germany
E-mail: tim.schroeder@physik.hu-berlin.de
J. M. Bopp, T. Schröder
Ferdinand-Braun-Institut gGmbH
Leibniz-Institut für Höchstfrequenztechnik
12489 Berlin, Germany
M. Plock, S. Burger
Zuse Institute Berlin (ZIB)
14195 Berlin, Germany
S. Burger
JCMwave GmbH
14050 Berlin, Germany

1. Introduction

Photon losses play a critical role in realizing optical quantum technologies.[1,2] In quantum communication protocols and optical one-way quantum computing, the losses must be as low as possible.[3,4] Losing photons in long-distance quantum communication degrades information transfer rates and limits the maximal communication distance to approximately 100 km.[5] This distance cannot be extended by classical signal amplification due to the no-cloning theorem.[6] However, quantum repeaters overcome the no-cloning theorem by exploiting entanglement between a stationary atom-like system and photons acting as 'flying qubits'.[3,7] Therefore, the repeaters require an interface between the atom-like system and photons. A photonic crystal cavity generally lies at the heart of such an interface. It enhances the light-matter interaction by means of the Purcell effect and thus the emitter's emission rate.[8–10] Likewise, the cavity improves photon collection efficiencies, in turn reducing photon losses.[11] Although significant effort has been spent toward controlling and increasing light-matter interaction,[1,11] it remains an open question how to design interfaces that provide photon collection efficiencies required by next generation quantum repeater protocols.[3]

In this work, we propose such a nanophotonic emitter-to-fiber interface based on a novel 'Sawfish' design (**Figure 1**). It couples the Purcell-enhanced emission of a solid-state quantum emitter via i) the nanocavity and ii) adiabatic mode conversion from a propagating Bloch into a waveguide mode iii) into a fiber. The Sawfish cavity design offers several advantages compared to present photonic crystal cavity designs. Unlike the multitude of existing cavity geometries that rely on tiny hole-like features 'drilled' into a (suspended) waveguide[9,10,12,13] or on rectangular 'fishbone' segments with sharp edges,[14] the Sawfish cavity is based on smooth, large-size corrugation features and on a low-loss adiabatic taper region. Being inspired by 'alligator' photonic crystal waveguides,[15] the Sawfish geometry extends them to efficient cavities by introducing exponentiated sinusoidal corrugation features and by removing the alligator photonic crystal waveguide's atom-trapping slit. For gentle mode

**ADVANCED
SCIENCE NEWS**

www.advancedsciencenews.com

**ADVANCED
OPTICAL
MATERIALS**
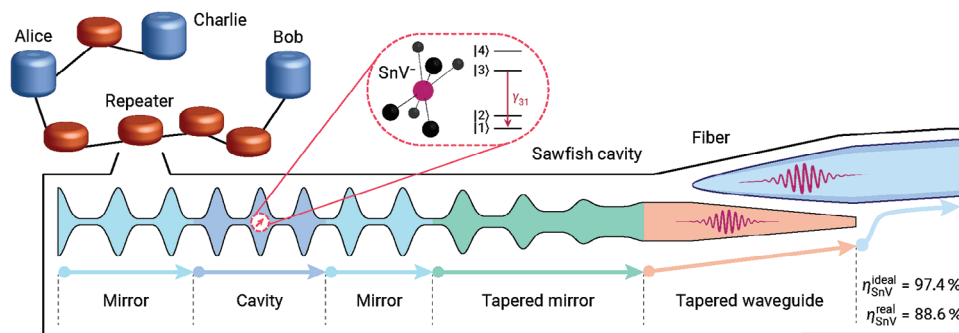
www.advopticalmat.de

Figure 1. Overview of the fiber-coupled Sawfish cavity as a building block for quantum networks. Several participants (blue nodes) communicate over a quantum network. Repeater stations (orange nodes) bridge long distances between the participants. Each repeater station consists of a quantum repeater involving SnV⁻ centers in diamond embedded in Sawfish cavities as photon sources. The SnV⁻ is enclosed by two mirror regions in the optical cavity's center enabling Purcell enhancement of the γ_{31} transition. In the sketch, the left mirror possesses a higher reflectivity than the right mirror. The latter transitions into a tapered region to firstly couple part of the emitted light adiabatically to a waveguide and second to a fiber.

confinement leading to high cavity quality factors Q as well as for adiabatic cavity-to-waveguide coupling, the cavity features have to be precisely adjusted.[11,16–18] Avoiding mode mismatch-induced scattering losses at cavity-waveguide interfaces is not straightforward since it necessitates arbitrary control of the cavity feature sizes.[19,20] Although strongly coupled cavity-to-waveguide designs have been introduced,[17] 'conventional' hole-based geometries suffer from fabrication difficulties in tapering off their hole diameters adiabatically.[19] In turn, fabricated hole-based Bloch waveguides do not provide arbitrarily smooth transitions into unperturbed waveguide regions. Our corrugated design overcomes this limit as it relies on open and relatively large features that can be tapered down adiabatically. Consequently, it enables near-unity emitter-to-waveguide and waveguide-to-fiber coupling efficiencies. The cavity-to-waveguide coupling efficiency reaches 99 %.

The Purcell factor F_P describes the ratio of a cavity-embedded quantum emitter's emission rate to its emission rate in bulk.[8] With F_P, we define the overall emitter-to-fiber coupling efficiency η as

$$\eta = \beta_C(F_P) \times \beta_{WG} \times \beta_F \times DW(F_P) \tag{1}$$

where $\beta_C(F_P) = F_P/(F_P + 1)$ is the probability to emit a photon into the cavity mode,[21,22] β_{WG} the cavity-to-waveguide coupling efficiency, and β_F the waveguide-to-fiber coupling efficiency. We restrict the emitter-to-fiber efficiency to the ratio of photons being emitted into the emitter's zero-phonon line (ZPL) by multiplication with the Debye-Waller factor $DW(F_P)$.[23,24] The Debye-Waller factor quantifies the fraction of ZPL to phonon sideband (PSB) emission and depends itself on the employed quantum emitter and the Purcell factor. Hence, η describes the overall probability that a single photon is emitted into a solid-state emitter's ZPL and then successfully transferred to an optical fiber.

As a case study, we consider the negatively-charged tin vacancy center in diamond (SnV⁻). The SnV⁻ possesses a ZPL at 484.3 THz and a comparably large ground state splitting of 850 GHz rendering it a promising optically-active spin emitter.[25,26] Our spin-photon interface, however, is applicable to a large variety of solid-state quantum emitters. This allows for its

integration with nanophotonic devices based on different material platforms.

In the following sections, we first introduce the Sawfish cavity design in detail. After optimizing the performance of the emitter-to-fiber coupling, we then explore how nanofabrication tolerances affect the cavity. We develop and apply a surrogate modeling procedure which yields information on how specific fabrication parameter distributions influence the expected performance. Vice versa, the procedure reveals requirements on parameter distributions to make a performance parameter, like the Purcell factor, exceed a certain threshold. To showcase this modeling technique, we discuss the effect of non-ideal emitter placement and deviations in the cavity's thickness, width, and side wall angles. Besides gauging the robustness of the Sawfish design in presence of deviations from its ideal configuration, surrogate modeling aids to anticipate which aspects of the device fabrication require the highest precision. To achieve comparability with experimentally realized cavity designs, we furthermore consider realistic cavity parameters. In particular, we employ one of the highest experimentally achieved diamond photonic crystal cavity quality factors Q to date reported by S. Mouradian et al. to benchmark our design.[12] Next, we demonstrate how the cluster state generation rate in a recent one-way quantum repeater protocol by J. Borregaard et al.[3] directly benefits from prospective improvements in nanofabrication methods. Finally, we study the performance of the Sawfish cavity loaded with a variety of color centers such as the negatively-charged nitrogen (NV⁻)[27] or negatively-charged group-IV[28] vacancy centers in diamond.

2. Results and Discussion

We first outline the physical considerations, which inform the Sawfish cavity design. Then, a tapered mirror region is added to the cavity to adiabatically convert the confined cavity mode into a traveling waveguide mode. This mode is next transferred to a tapered fiber. Ultimately, we investigate the cavity's robustness under experimental state-of-the-art conditions such as non-optimal emitter placement and fabrication tolerances, as well as its impact on a modern quantum repeater protocol.
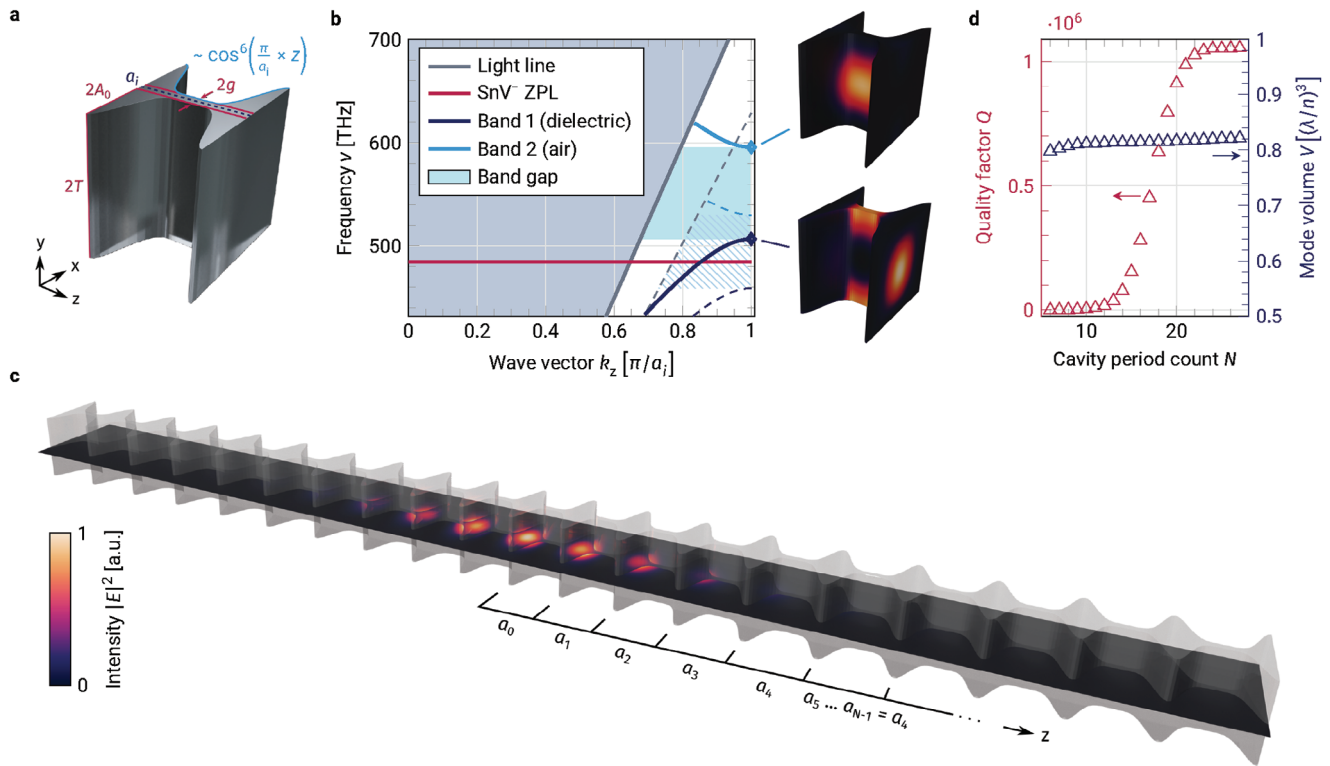
Figure 2. Sawfish unit cell and cavity design. a) Unit cell of the Sawfish cavity with its characteristic parameters. a_i describes its lattice constant, $2T$ its thickness, $2A_0$ the (untapered) amplitude of a $\cos^6$ function offset by g from the $x = 0$ symmetry plane (dashed line) defining the unit cell's profile. b) Band diagram of a periodic array of Sawfish unit cells showing TM-like modes. Light modes inside the light cone (gray-shaded area given by $v \geq c|k|$ with c being the speed of light) may escape the structure. Other components propagate as Bloch modes indicated by blue solid and dashed lines for lattice constants $a_0 = 200$ nm and $a_4 = 238.5$ nm, respectively. Between the fundamental Bloch mode (dark blue line) and the next higher air mode (light blue line), there is a 88.7 THz-wide bandgap (blue-shaded area) for a unit cell lattice constant of a_0. For this lattice constant, the SnV$^-$ ZPL emission (red line) is guided as the fundamental mode. Emission is suppressed for a unit cell lattice constant of a_4 by the ZPL falling into the bandgap (blue-dashed area). The insets portray the electric field intensity of the modes highlighted with blue diamonds. c) Sawfish cavity geometry. The two symmetric halves of the cavity consist of N concatenated Sawfish unit cells each with lattice constants increasing from a_0 to a_4. The center plane displays the electric field intensity. d) Convergence behavior of the cavity's quality factor Q (red) and its mode volume V (blue) depending on the amount of concatenated unit cells counting from on the cavity's central $z = 0$ symmetry plane.

2.1. Cavity Design

For constructing a freestanding cavity based on corrugation features, a periodic structure formed by the cavity's unit cell must result in a photonic bandgap. To reliably suppress the transmission of light around its center frequency, the bandgap has to be large enough. We perform eigenmode simulations to determine the Sawfish unit cell's dispersion properties and to identify bandgaps centered around the SnV$^-$ ZPL. For diamond with a refractive index of $n = 2.41$ at 484.3 THz,[29] we find that a unit cell with lattice constant a_i and a sinusoidal corrugation along the z direction proportional to $\cos^e(\pi/a_i \times z)$ with $e = 2$ (parameters as indicated in **Figure 2a**) yields a gap-midgap ratio of only 7.8 %. Raising the exponent e increases the gap-midgap ratio dramatically due to a higher refractive index contrast between the unit cell's edges and its center. For $e = 6$, with all other parameters unchanged, a gap-midgap ratio of 16.1 % is obtained. We choose $e = 6$ since larger exponents do not further improve the bandgap significantly. A larger exponent would instead reduce the distance between an emitter located at the center of one of the unit cell's rectangular interfaces and the unit cell's curved surface. In turn, a small

emitter-surface distance would potentially promote undesired interactions between the emitter's dipole and surface charges.[30,31]

The blue solid and dashed lines in Figure 2b show the photonic band diagram for a periodic structure built by concatenating unit cells with lattice constants $a_0 = 200$ nm and $a_4 = 238.5$ nm, respectively. Here, the remaining parameters are $T = 133$ nm, $A_0 = 65$ nm, and $g = 11$ nm. The unit cells are optimized to maximize the bandgap, to permit the transmission of the SnV$^-$ ZPL for the lattice constant a_0, and to prohibit the transmission for a_4. Larger gap widths g might increase the stability of fabricated devices in trade for slightly narrower bandgaps. Unit cells with lattice constants a_0 guide the ZPL emission in the form of a dielectric mode that is mostly confined in the diamond material. Larger lattice constants shift the band diagram toward lower frequencies eventually making the ZPL emission approach the bandgap's center. Unit cells with lattice constant a_4 hence act as mirror elements. The cavity's center region gently confines a light mode in the vicinity of the SnV$^-$ ZPL if N unit cells with increasing lattice constants $a_0, a_1, ..., a_{N-1}$ are arranged on either side around the cavity's $z = 0$ symmetry plane. We reach the highest quality factor $Q = 1.06 \times 10^6$ with $[a_1, a_2, a_3] = [207.0$ nm, 217.9 nm, 228.4 nm$]$
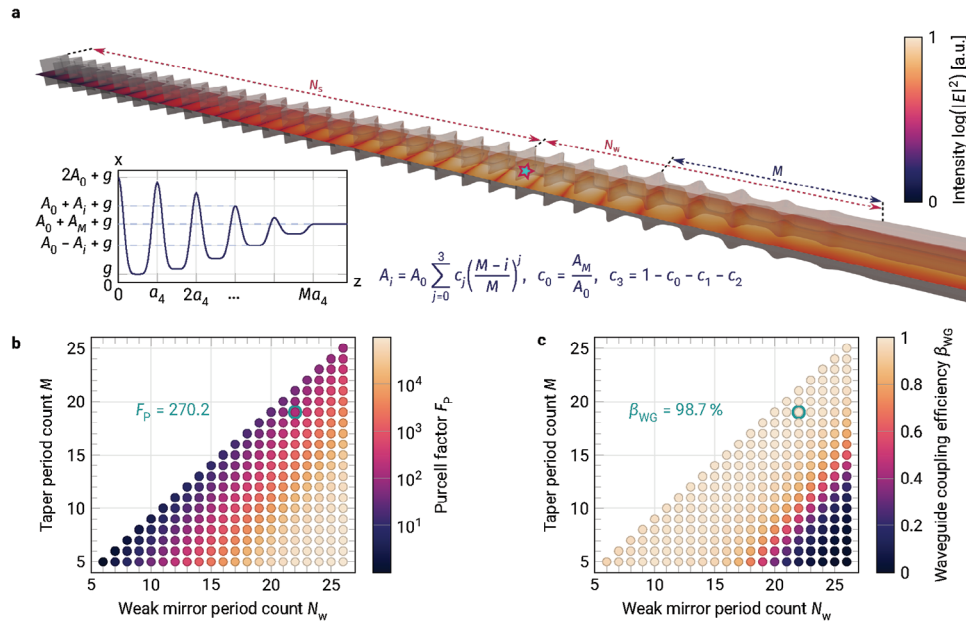
**ADVANCED
SCIENCE NEWS**

www.advancedsciencenews.com

**ADVANCED
OPTICAL
MATERIALS**

www.advopticalmat.de

Figure 3. Waveguide-coupled Sawfish cavity design. a) The waveguide-coupled cavity consists of a strong mirror region of N_s unit cells with amplitude $2A_0$ left of the emitter indicated by the small star and a weak mirror region of N_w unit cells right of the emitter. The amplitudes $2A_i$ ($i \in [0, M]$) of the unit cells within the weak mirror region stay constantly at $2A_0$ for $N_w - M$ periods (beginning at the emitter) and taper down to the final amplitude $A_0 + A_M$ according to a third-order polynomial with coefficients c_j along the taper region M as depicted in the inset. The center plane displays the logarithm of the electric field intensity. b) Purcell factor F_P and c) waveguide coupling efficiency β_{WG} depending on the amount of unit cells forming the weak mirror and on the length of the taper region. N_s is fixed to 23. The data point highlighted in green denotes the configuration with the highest waveguide coupling efficiency. For each point, the [010]-oriented dipole's emission frequency has been set to the respective configuration's resonance.

in addition to a_0 and a_4 as mentioned above. a_5 to a_{N-1} are equal to a_4. Figure 2c visualizes the resulting electric field intensity in the cavity.

With the cavity's quality factor Q and its mode volume V, the overall emission rate of an emitter embedded into the cavity is increased by the Purcell factor $F_P \sim Q/V$ compared to its bulk emission rate.[8] A high quality factor in combination with a small mode volume therefore also raises the ZPL emission through an increased Debye-Waller factor $DW(F_P)$ and hence the emitter-to-fiber coupling efficiency η. Since each mirror element constituting the cavity contributes to a photonic potential barrier,[32] the quality factor rapidly increases for a critical amount of mirror elements as soon as tunneling of the cavity mode through the barrier approaches full suppression (Figure 2d). In our case, simulation-based state-of-the-art quality factors above 1×10^6 can be reached for $N > 20$.[12,33] The mode volume stays comparably low at $0.8 \, (\lambda/n)^3$ over the full range of investigated cavity period counts with λ being the individual wavelength of the respective cavity's resonance mode.

2.2. Cavity to Waveguide Coupling

Controlled out-coupling of the light mode confined in the cavity requires to weaken the cavity's reflectivity at one side of the emitter. In addition to lowering the reflectivity, we damp the amplitude of the corrugation features to adiabatically transfer the Bloch mode to a waveguide mode. Hence, an asymmetric cavity consisting of a strong and a weak mirror needs to be constructed. The strong mirror consists of N_s unit cells, the weak mirror of N_w

cells, respectively. The unit cells forming the weak mirror stay at a constant amplitude for $N_w - M$ periods until they taper down to a waveguide with a final total width $2(A_0 + A_M + g)$ over M periods according to the profile given by a third-order polynomial as stated in **Figure 3a**. A_M determines the waveguide's width after the tapered region. Barely affecting the cavity-to-waveguide coupling efficiency, it can be chosen to fit the subsequent fiber coupling requirements. We find by Bayesian optimization that a profile following a third-order-polynomial with coefficients $c_1 = 0.275$, $c_2 = 2.243$ and $A_M = 2.5$ nm is most efficient for our Sawfish geometry.[34]

For now, we focus on an ideal system with $N_s = 23$ and a dipole perfectly overlapping with the desired TM-like mode. A corresponding untapered symmetric cavity with $N = 23$ possesses a central frequency $\omega_c = 2\pi \times 484.70$ THz and an intrinsic scattering loss rate $\kappa_s = \omega_c/Q_s = 2\pi \times 463.8$ MHz (Figure 2). By choosing weak mirrors with different amounts of contributing unit cells N_w and different taper lengths M, the Purcell factor F_P and thus the emitter-cavity cooperativity (given by $F_P/2$)[35] can be adjusted over a wide range (Figure 3b). The waveguide coupling efficiency β_{WG} defined as the ratio of the Poynting vector integrated over the waveguide's end facet to the Poynting vector integrated over the entire computational domain remains at approximately $\beta_{WG} = 99\%$ over the parameter range significant for cooperativity tuning (Figure 3c). In turn, the Purcell factor might be arbitrarily chosen without causing additional scattering losses at the tapered region.

For each weak mirror period count N_w, there is a range of taper lengths which maximize both, the Purcell factor as well as the waveguide coupling efficiency. In contrast, the Purcell factor
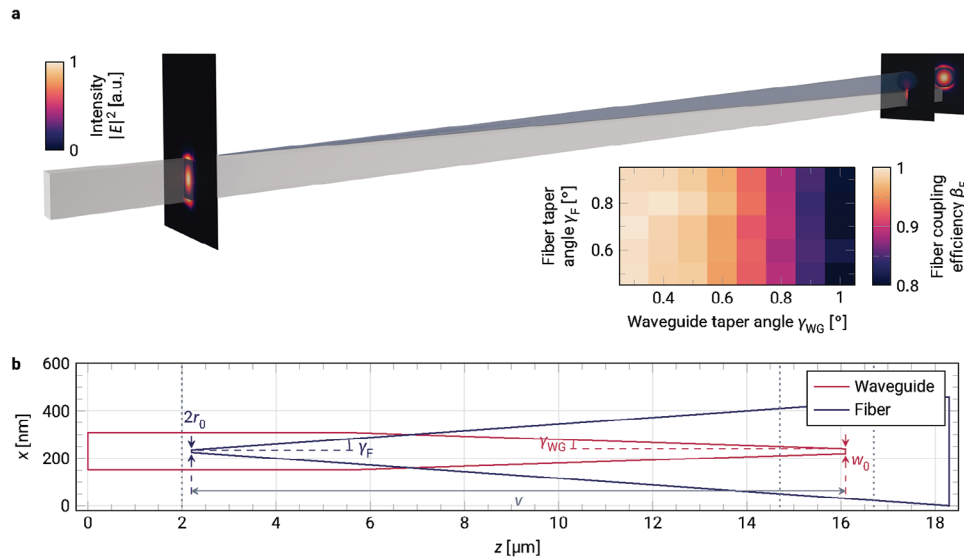
Figure 4. Fiber-coupling of the waveguide attached to the Sawfish cavity. a) Simulated model of the tapered waveguide (gray-shaded) coupled to a tapered fiber placed on top (blue-shaded) including three cross-sectional views of the electric field intensity. The inset shows the dependence of the waveguide-to-fiber transmission β_F on the taper angles as defined in (b). The length of the overlapping region v has been optimized for each set of angles. b) Top view of the waveguide-fiber system. A diamond waveguide (red) with a thickness of $2T$ and an initial total width of $2(A_0 + A_M + g)$ as it is attached to the Sawfish cavity is tapered down under an angle γ_{WG} to a final width w_0. A tapered fiber (blue) modeled as a conical frustum with a final radius r_0 and a taper angle γ_F overlaps the tapered waveguide for a length v measured from the waveguide's tip. Gray dotted lines denote z coordinates of the planes displaying cross-sectional intensities in (a).

drops if M is chosen too high leading to an excessive cavity-to-waveguide loss rate. If M is chosen too low, F_P increases, but β_{WG} drops for the cavity-to-waveguide loss rate being reduced to the intrinsic loss rate κ_s. Such dependencies emphasize the need to thoroughly design tapered regions interfacing cavities with waveguides and not to neglect their influence on the cavities themselves.

To experimentally investigate group-IV defects in diamond like the SnV$^-$, often highly pure CVD diamond samples are ion-implanted and subsequently annealed.[9,10,25] The respective off-the-shelf diamond substrates are usually cut along the crystallographic [100] direction causing dipoles to enclose an angle of 54.7° with each cartesian axis ([111] direction).[36,37] Consequently, for modeling a realistic scenario, the effect of rotating the dipole embedded in our Sawfish design within a plane spanned by the [111] ($\alpha = 54.7°$) and e.g., the [010] ($\alpha = 0°$) direction has to be examined. We observe that the Purcell factor follows a $F_P \sim g^2 \sim \cos^2(\alpha)$ law since the coupling constant g depends on a scalar product between the cavity mode at the dipole's position and its orientation. A realistic dipole orientation reduces the Purcell factor to approximately 33 % of its value obtained for an ideal orientation. Remarkably, the waveguide coupling efficiency is hardly affected. It is slightly reduced to 99.8 % of its ideal value (see Supporting Information).

2.3. Waveguide to Fiber Coupling

Aiming to eventually couple light generated by a cavity-coupled emitter into a fiber network, we show that the waveguide attached to our Sawfish cavity allows for efficient fiber coupling. We use a waveguide-fiber interface according to T. G. Tiecke et al.[38] The

waveguide narrows down to its final width $w_0 = 5\,\text{nm}$ under an angle γ_{WG}. A conical fiber tip with a core refractive index of $n = 1.463$ tapered down to a radius $r_0 = 5\,\text{nm}$ under an angle γ_F is put on top of the waveguide overlapping it for a length v (**Figure 4**).

A waveguide-to-fiber transmission β_F of up to $\beta_F = 99.4\,\%$ is reached for $\gamma_{WG} = 0.3°$, $\gamma_F = 0.7°$, and an overlap $v = 20\,\mu\text{m}$ considering realistic taper and fiber end dimensions (inset in Figure 4a). The effective refractive index of the optical mode traveling through the combined system initially resembles the effective refractive index of the fundamental waveguide mode, but approaches the one of the fundamental fiber mode emphasizing successful evanescent coupling (see Supplementary Information).[38]

2.4. Surrogate Modeling of Fabrication Uncertainties

Until this point, our investigation of the Sawfish cavity was mainly based on ideal conditions disregarding scattering losses due to e.g., fabrication tolerances or rough surfaces. To explore how fabrication tolerances impact the Sawfish cavity's performance, we perform Monte Carlo sampling on a surrogate model. Once the surrogate model is trained with computationally expensive simulation data for a set of fabrication parameters, any uncertainty distribution of the selected parameters can be evaluated quickly (see Supporting Information). Lacking the need for further computationally expensive simulations when exchanging the uncertainty distributions renders the surrogate modeling procedure a powerful tool to efficiently analyze the impact of fabrication tolerances on any nanostructure. From now on, we consider realistically [111]-oriented dipoles.
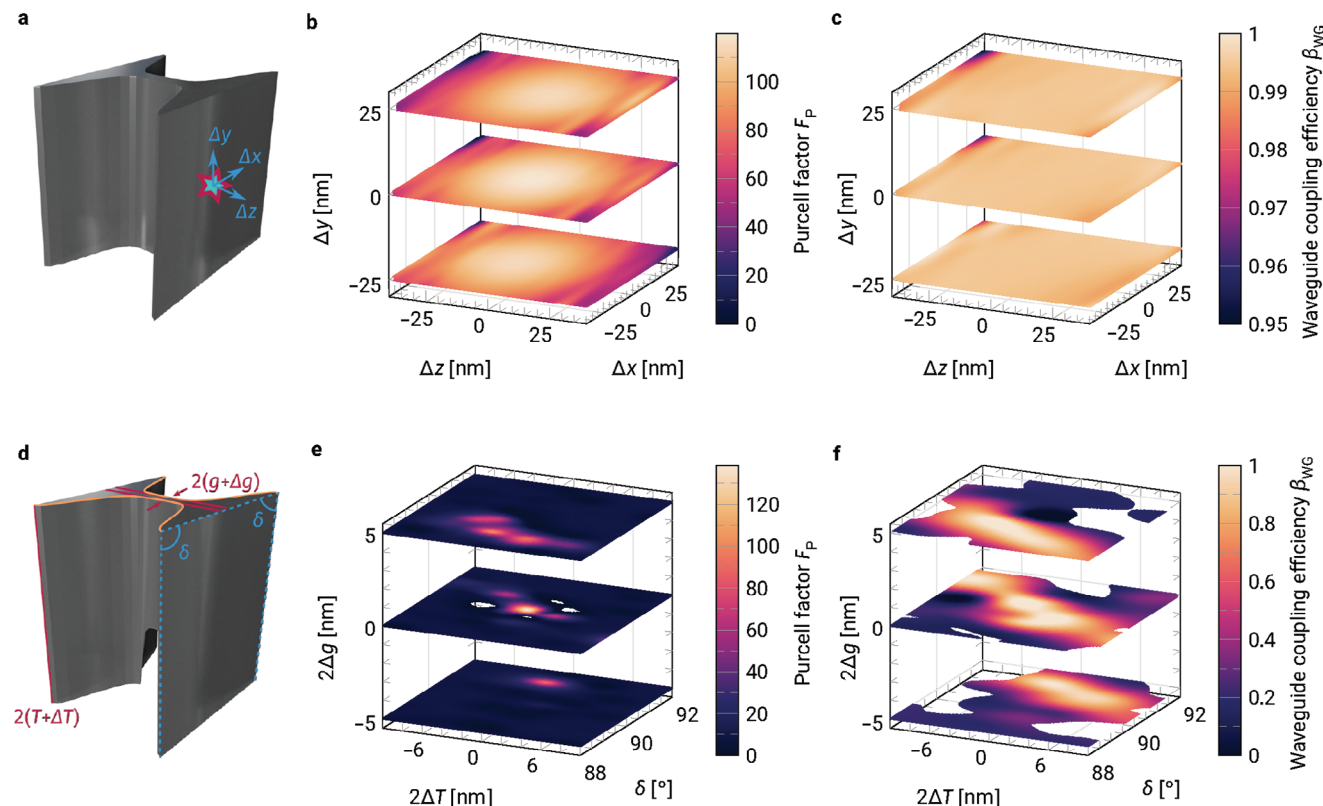
Figure 5. Influence of dipole displacement and fabrication tolerances. a) For ideal fabrication parameters, the [111]-oriented dipole (indicated as a star) is displaced along the cartesian axes by distances Δx, Δy, and Δz measured from the cavity's center point. b, c) Colors describe the resulting Purcell factor F_P (b) and waveguide coupling efficiency β_{WG} (c) for displaced dipoles. d) With an ideally positioned, [111]-oriented dipole, fabrication geometry parameters are altered. The cavity's thickness is varied by $2\Delta T$ and its gap width by $2\Delta g$. Its side wall angle δ is allowed to deviate from 90°. Orange lines denote edges for which the influence of rounded corners is investigated. e, f) Colors describe the Purcell factors F_P (e) and waveguide coupling efficiencies β_{WG} (f) for deviations from ideal fabrication geometry parameters. Predictions by the surrogate model with high uncertainties have been removed from the displayed planes.

With a dipole displaced by distances [Δx, Δy, Δz] scattering around a zero mean value (ideal dipole position) with standard deviations of 25 nm each (**Figure 5a**), we obtain $\overline{F}_P = (91.4 \pm 3.2)^{+18.3}_{-26.0}$ and $\overline{\beta}_{WG} = (0.9863 \pm 0.0014)^{+0.0003}_{-0.0014}$ as median values for the Purcell factor and the waveguide coupling efficiency, respectively. The values' uncertainties denote combined Monte Carlo and surrogate uncertainties. Lower and upper bounds indicate lower and upper standard deviations of the values' distributions. Figure 5b,c presents the dependencies $F_P(\Delta x, \Delta y, \Delta z)$ and $\beta_{WG}(\Delta x, \Delta y, \Delta z)$ as predicted by the surrogate model. While the Purcell factor only diminishes for high deviations along the x- and z-axis, it is even less affected by dipoles displaced along the y-axis. This effect is understandable considering the cavity mode profile (inset in Figure 2b). The electric field spreads further in y-direction compared to the other directions causing the mode overlap to be less affected by dipole displacements in this direction. In contrast, β_{WG} is hardly influenced by any displacement.

Likewise, we investigate fabrication geometry parameters [ΔT, δ, Δg] distributed around their ideal design values [0 nm, 90°, 0 nm] (Figure 5d). Rounded corners along the edges highlighted with orange lines in Figure 5d, as another relevant parameter, do not have any influence up to a corner rounding radius of at least 5 nm. Figure 5e, f displays predictions of the single fabrication parameters' impact on F_P and β_{WG}, respectively. In general, β_{WG} is affected much less than F_P by fabrication tolerances. However, the Purcell factor strongly depends on the correct choice of fabrication parameters. This is the case since fabrication uncertainties shift the unit cells' band structures away from the cavity condition rapidly. The system then becomes a pure waveguide supporting Bloch modes, but no resonant cavity mode, which is expressed in regions with low Purcell factors but still high waveguide coupling efficiencies. Some parameters reveal correlations. For instance, a cavity with a lowered side wall angle works efficiently if the gap is enlarged at the same time. Thus, we emphasize the need for a precise model that takes the predetermined measurement uncertainties into account to achieve controllable nanofabrication.

For standard deviations [0.8 nm, 0.1°, 0.8 nm] of the fabrication geometry parameters [ΔT, δ, Δg], we obtain $\overline{F}_P = (48.5 \pm 26.5)^{+48.0}_{-33.5}$ and $\overline{\beta}_{WG} = (0.929 \pm 0.054)^{+0.057}_{-0.141}$. $\overline{F}_P$ and $\overline{\beta}_{WG}$ describe median values for the ratio of 95 % working Sawfish cavities (see Supporting Information) assuming the given fabrication tolerances and cavity tuneability within a frequency range between 483.6 and 485.1 THz.
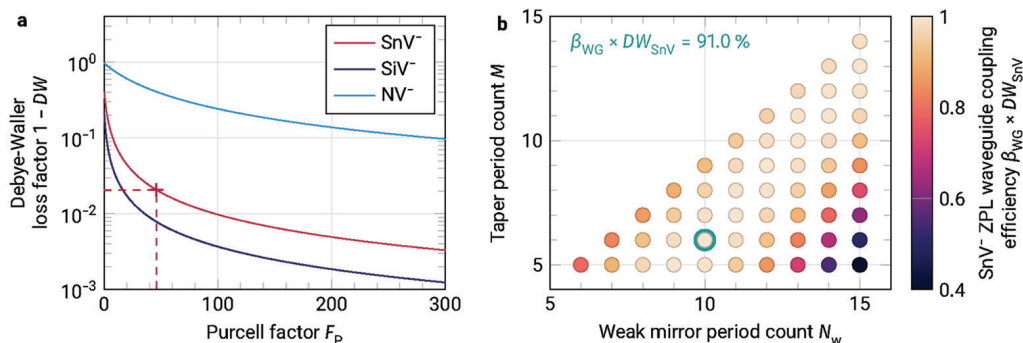
**ADVANCED
SCIENCE NEWS**

www.advancedsciencenews.com

**ADVANCED
OPTICAL
MATERIALS**

www.advopticalmat.de

Figure 6. Debye-Waller factor and ZPL waveguide coupling efficiency for a [111]-oriented SnV⁻ and realistic losses. a) Dependence of different diamond defect centers' Debye-Waller factors DW on the Purcell factor F_P. The red cross at $F_P = 46.4$ highlights the SnV⁻-based Sawfish cavity configuration with the highest efficiency for realistic losses (green circle in (b)). The GeV⁻'s Debye-Waller factor is not depicted since it matches the SnV⁻'s curve. b) SnV⁻ ZPL waveguide coupling efficiency $\beta_{WG} \times DW_{SnV}$ for different amounts of unit cells forming the weak mirror and different lengths of the taper region. The encircled data point denotes the configuration with the highest efficiency. The dipole has been adjusted to the cavity's resonance for each point.

2.5. Experimental State-of-the-Art Conditions

In the previous section, we assessed how fabrication tolerances explicitly arising from displaced dipoles or deviating fabrication parameters affect the Sawfish cavity. In this section, we instead investigate the influence of reduced quality factors without defining the origin of the respective additional loss channel. Combining both approaches allows to relate desired quality factors and thus also Purcell factors to requirements on dipole displacement distributions and fabrication tolerances.

To represent experimental state-of-the-art conditions without modeling every possible fabrication uncertainty (including surface roughness) explicitly, we consider a short and lossy cavity as a realistic model of a cavity with nanofabrication-induced losses. More specifically, by turning an ideal cavity's strong mirror more transparent, we insert losses which equal the losses caused by fabrication imperfections. In this way, we imitate a cavity with realistic losses. We fix the quality factor of an untapered symmetric Sawfish cavity to $2Q \approx 17000$ by reducing its length to $N_s = N_w = 11$ (Figure 2d). This value is on the order of magnitude of a currently fabricated photonic crystal cavity.[12] The factor two takes into account that half of the light leaving a symmetric cavity will be collected through the weak mirror of a corresponding tapered asymmetric cavity. The collected part does not contribute to the losses. It is coupled to the attached waveguide instead. Next, we introduce a tapered region to render the cavity with intrinsic scattering losses and a realistic [111]-oriented dipole asymmetric and to couple it to a waveguide. We optimize the asymmetric cavity's taper region parameters N_w and M. For the best resulting taper region as highlighted in **Figure 6**, we obtain $F_P = 46.4$ and $\beta_{WG} = 92.9\%$. Both values agree well with the $\overline{F}_P$ and $\overline{\beta}_{WG}$, which we obtain for fabrication geometry parameters $[\Delta T, \delta, \Delta g]$ distributed as described in Section 2.4. Hence, surrogate modeling allows to directly map a desired quality factor to requirements on fabrication tolerances.

The Purcell factor directly determines β_C, as well as the Debye-Waller factor DW_{SnV}. With the emission rate into the ZPL γ_{31} (inset in Figure 1), the emission rate into the PSB γ_{PSB} and the SnV⁻'s natural Debye-Waller factor in bulk $DW^0_{SnV} \approx 60\%$,[37] its Debye-Waller factor in presence of Purcell enhancement becomes

$$DW_{SnV}(F_P) = \frac{\gamma_{31}F_P\left(1 - DW^0_{SnV}\right) + DW^0_{SnV}\gamma_{PSB}}{\gamma_{31}F_P\left(1 - DW^0_{SnV}\right) + \gamma_{PSB}} \tag{2}$$

as plotted in Figure 6a (see Supporting Information). With an optimized taper region (Figure 6b), we estimate the overall emitter-to-fiber collection efficiency of a lossy realistic system for the SnV⁻ ZPL to $\eta^{real}_{SnV} = 88.6\%$ neglecting further systemic optical losses.[11] For ideal conditions (configuration highlighted in Figure 3b, c), the collection efficiency rises to $\eta^{ideal}_{SnV} = 97.4\%$.

2.6. Application to Quantum Repeaters

One-way quantum repeaters use multi-photon encoding and quantum error-correction to protect quantum information from losses and other errors.[39–45] The amount of photons N_{ph} required for such multi-photon entangled states strongly depends on the employed encoding protocol and the efficiency of transferring photons from one network node to adjacent nodes. To extend the possible quantum communication distances, there is a need for efficient quantum repeaters with minimal resource requirements. Thus, we now benchmark the Sawfish spin-photon interface performance applying it to the modern one-way quantum repeater protocol recently proposed by Borregaard et al.[3] To reach reasonable operational conditions, the protocol requires node-to-node (emitter-to-detection) efficiencies of around 95% depending on the system error rate ϵ_r. The emitter-to-detection efficiency includes the photon generation and fiber coupling on the sender and the photon detection efficiency on the receiver site. In turn, the photon generation involves the fiber-coupled Sawfish cavity.

We assess the performance evaluating the cost function defined by Borregaard et al.[3]

$$C = \frac{1}{\Gamma_{tcs} f p_{trans}(\eta)} \frac{m L_{att}}{\tau_{ph} L} \tag{3}$$

**ADVANCED
SCIENCE NEWS**

www.advancedsciencenews.com

**ADVANCED
OPTICAL
MATERIALS**

www.advopticalmat.de

as a function of the emitter-to-fiber collection efficiency η (Equation (1)). Γ_{tcs} is the tree-cluster state generation rate, f the secret-bit fraction of the transmitted qubits,[46] $p_{trans}(\eta)$ the transmission probability that depends on η and on the tree-cluster state configuration, m the number of repeater stations, L_{att} the optical fiber attenuation length, τ_{ph} the photon emission time, and L the total communication distance. $1/C$ can be interpreted as the secret key rate in units of the photonic qubit emission time per repeater station and per attenuation length for a given total distance L. The detection efficiency is implicitly included in $p_{trans}(\eta)$ (see Supporting Information for details). η drastically affects the cost function C (**Figure 7**a) and therefore the cluster state size N_{ph} (Figure 7b) that is best suited for distributing a secret key between two distant parties. The strong dependence on the emitter-to-fiber efficiency motivates optimized spin-photon interface designs. While C is smoothly decreasing, N_{ph} decreases stepwise with increasing system efficiency underlining that photon losses have to be reduced to a particular threshold. The cost reduction with increasing emitter-to-fiber efficiency becomes intuitive considering that lower losses result in fewer photons needed for error correction. Whereas higher reencoding errors raise the cost function, higher overall emitter-to-fiber efficiencies drastically reduce it in every case. This result further reinforces the relevance of improving the overall system efficiency in the presence of higher reencoding errors. Reducing the intrinsic cavity scattering losses from a state-of-the-art value towards ideal conditions, the tree-cluster state generation rate Γ_{tcs} related to the cost function by $C \sim 1/\Gamma_{tcs}$ (see Supporting Information) rises by over an order of magnitude (blue curve in Figure 7c). Even in case of an efficiently fiber-coupled photon source without Purcell enhancement, this observation remains almost unchanged (red curve in Figure 7c). In presence of Purcell enhancement and intrinsic scattering losses of $2Q \approx 156000$ corresponding to $\eta_{SnV} = 94.7\%$, the state generation rate rises from 1.1 to 12.5 MHz. Though, already with $\eta_{SnV}^{real} = 88.6\%$ implied by an intrinsic state-of-the-art quality factor of $2Q \approx 17000$,[12] the state generation rate reaches the MHz regime.

Considering these results, we conclude that expected improvements in diamond nanofabrication in combination with diamond vacancy centers embedded in Sawfish cavities put the optical requirements of the one-way repeater approach discussed here within reach.

3. Conclusion

We introduced and optimized a waveguide-coupled 'Sawfish cavity' and estimated the overall probability of successfully transferring ZPL photons of an embedded SnV− to an optical fiber. For ideal conditions, a probability of $\eta_{SnV}^{ideal} = 97.4\%$ was obtained which dropped for state-of-the-art cavity losses only slightly to $\eta_{SnV}^{real} = 88.6\%$. Furthermore, we showcased that tailoring the photonic potential barrier formed by the Sawfish cavity's taper region allows for waveguide-coupled cavities with distinct cooperativities without reducing their cavity-to-waveguide coupling efficiencies. Applying a Monte Carlo sampling method performed on a surrogate model enabled us to map specific cavity losses to a set of corresponding fabrication tolerances. Even taking these scattering losses into account, the overall efficiency η_{SnV}^{real} exceeds to date findings in recent work for hole-based photonic crys-
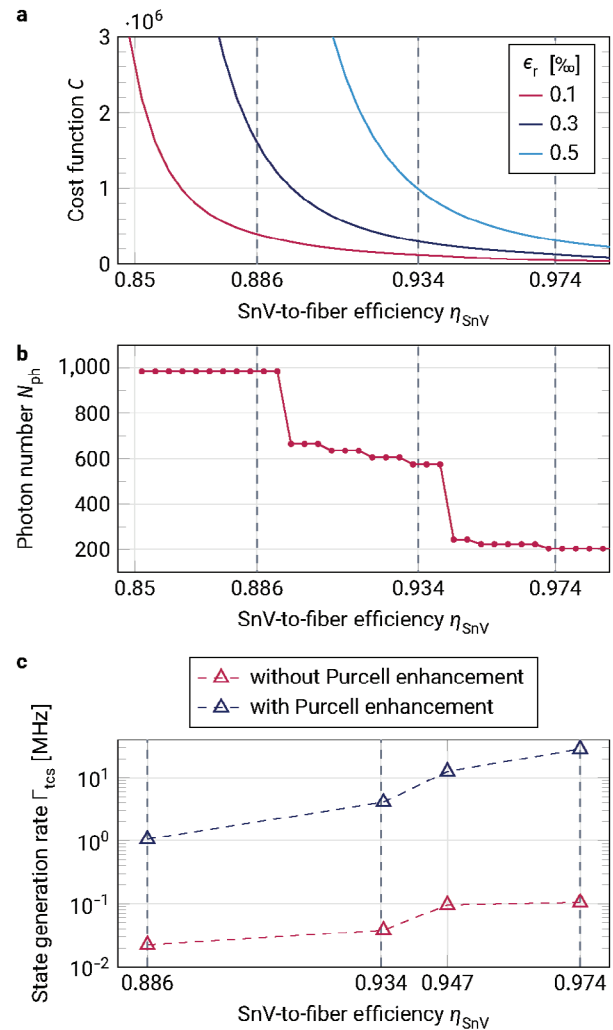
Figure 7. Efficiency of a one-way quantum repeater scheme by J. Borregaard et al.[3] based on a SnV−-loaded Sawfish cavity. a) Cost function C (Equation (3)), b) photon number N_{ph} required for tree-cluster resource states, and c) tree-cluster state generation rate Γ_{tcs} (see Supporting Information) as functions of the SnV-to-fiber efficiency η_{SnV} (Equation (1)). The cost function is shown for different reencoding errors ϵ_r, while the reencoding error is fixed to $\epsilon_r = 0.1\%_0$ for the photon number and the tree-cluster state generation rate. Vertical dashed lines at $\eta_{SnV}^{real} = 88.6\%$ correspond to state-of-the-art cavity quality factors $2Q \approx 17000$ (see Section 2.5), lines at $\eta_{SnV} = 93.4\%$ to $2Q \approx 76000$, which is expected to be within reach in the close future, and lines at $\eta_{SnV}^{real} = 97.4\%$ to an idealized cavity design. Red and blue dashed lines serve as guides to the eye.

tal cavities.[11] We highlighted the benefits of extremely efficient spin-photon interfaces by applying the Sawfish cavity to the one-way quantum repeater scheme of J. Borregaard et al.[3] The repeater nodes' resource requirements, like the tree-cluster state sizes, reduced significantly. As a consequence, the Sawfish cavity provides fabrication uncertainty-tolerant near-unity collection of light generated by e.g., a diamond color center through an adiabatic cavity-to-waveguide followed by an adiabatic waveguide-to-fiber transition.

Although the Sawfish cavity has been optimized for a SnV− center in diamond to demonstrate its properties and perfor-

**ADVANCED
SCIENCE NEWS**

www.advancedsciencenews.com

**ADVANCED
OPTICAL
MATERIALS**

www.advopticalmat.de

Table 1. Overall emitter-to-fiber efficiencies for different defect centers in diamond assuming the same waveguide (β_{WG}) and fiber (β_F) coupling efficiencies as found by simulations for the SnV⁻ and either ideal ($F_P = 270.2$) or realistic state-of-the-art ($F_P = 46.4$) conditions. All efficiencies refer to the respective emitter's ZPL emission. τ^0 denotes the considered excited state lifetime in bulk diamond. τ^{ideal} and τ^{real} denote the calculated Purcell-enhanced lifetimes for ideal and realistic conditions, respectively.

	NV⁻	SiV⁻	GeV⁻	SnV⁻
τ^0 [ns]	12.2[48]	1.7[49]	3.8[50]	4.5[51]
τ^{ideal} [ns]	1.3	0.01	0.03	0.04
τ^{real} [ns]	5.1	0.07	0.19	0.23
DW^0 [%]	3[52]	80[53]	60[54]	60[37]
DW^{ideal} [%]	89.3	99.9	99.6	99.6
DW^{real} [%]	59.4	99.2	98.0	98.0
η^{ideal} [%]	87.4	97.6	97.4	97.4
η^{real} [%]	53.8	89.7	88.6	88.6

mance, we emphasize that the cavity design is adaptable to other diamond defect centers, as well as to other material platforms hosting a quantum emitter. Scaling the cavity's dimensions adjusts its resonance frequency.[47] Assuming the same cavity-to-waveguide and waveguide-to-fiber coupling efficiencies but the respective Debye-Waller factors, we present the expected system efficiencies for different diamond defect centers in **Table 1**. Clearly, the Sawfish cavity raises the bulk Debye-Waller factor DW^0 of every emitter and thus provides high system efficiencies not only for the SnV⁻.

Having demonstrated the advantages of the Sawfish cavity in simulations, its performance after diamond nanofabrication and as a building block for photonic integrated circuits demands further investigation. Concerning fabrication tolerances, predictions of the trained surrogate model necessitate verification by analyzing batches of fabricated cavities. To this point, it is not known to what extent rough surfaces possibly caused by diamond etching affect the Sawfish cavity's performance.

Optical losses in any spin-photon interface lead to a tremendously reduced efficiency in quantum information processing applications. This especially holds if an emitter has to repeatedly mediate entanglement for resource states involving hundreds of photons or if quantum memories become involved.[3,55] Whereas there are most efficient photon detectors with 99.5 % detection efficiency nowadays,[56] equally efficient spin-photon interfaces are still missing. Our system fulfills the prerequisites of the PEPSI scheme used to map photonic polarization-encoded qubits onto solid-state spins: even with intrinsic state-of-the-art scattering losses, it enables a spin-photon interface exceeding the needed efficiency of 83 % and allowing for cooperativity tuning.[1] Consequently, we deem the Sawfish cavity design to be critical in interfacing quantum emitters and memories with near-unity efficiencies as required for scalable quantum networks.

4. Experimental Section

As a promising optically-active solid-state spin system, negatively-charged tin vacancy centers in diamond (SnV⁻) were examined exemplarily. Their ZPL emission at 484.3 THz was coupled to the Sawfish

cavities.[25] Debye-Waller factors were calculated according to a formalism by L. Li et al.[23] The system was investigated performing full 3d finite element (FEM) simulations with the software package JCMsuite.[57]

First, the geometry parameters of the Sawfish cavity's central unit cell, like its lattice constant a_0, its thickness $2T$, its amplitude $2A_0$, and its gap width $2g$ were chosen to establish a large enough photonic bandgap centered around the SnV⁻ ZPL. Based on eigenmode computations, the higher-order lattice constants a_i were then optimized for large quality factors using a Bayesian optimizer implemented in JCMsuite.[58] The same optimizer was employed for designing the cavity-waveguide and waveguide-fiber interfaces. Investigating electromagnetic energy fluxes originating from a single dipole emitter placed at the cavity's center allowed to analyze the system's efficiency. Furthermore, distributions of cavity design parameters were accounted for by performing Monte Carlo sampling on a surrogate model composed of Gaussian processes and trained by means of machine learning. Through the surrogate model, insights were gained into the cavity's robustness under displaced dipoles and fabrication tolerances. Finally, the optimized system efficiencies were applied to benchmark the potential performance of a one-way quantum repeater regarding the cost C, the required tree-cluster state size N_{ph}, and the tree-cluster state generation rate Γ_{tcs} following procedures detailed by J. Borregaard et al.[3] For details, see Supporting Information.

Supporting Information

Supporting Information is available from the Wiley Online Library or from the author.

Conflict of Interest

The authors declare no conflict of interest.

Author Contributions

J.M.B. designed the Sawfish cavity and its waveguide coupling. M.P. developed the procedure to analyze the effect of fabrication tolerances. T.T. simulated the waveguide-to-fiber coupling. G.P. applied the Sawfish cavity to quantum repeater protocols. T.S. conceived the project. S.B. and T.S. supervised it. All authors contributed to the manuscript.

Data Availability Statement

The data that support the findings of this study are available from the corresponding author upon reasonable request.

[1] K. C. Chen, E. Bersin, D. Englund, *npj Quantum Inf.* **2021**, 7, 2.

[2] T. Neuman, M. Eichenfield, M. E. Trusheim, L. Hackett, P. Narang, D. Englund, *npj Quantum Inf.* **2021**, 7, 121.

[3] J. Borregaard, H. Pichler, T. Schröder, M. D. Lukin, P. Lodahl, A. S. Sørensen, *Phys. Rev. X* **2020**, 10, 021071.

[4] R. Raussendorf, H. J. Briegel, *Phys. Rev. Lett.* **2001**, 86, 22.

[5] V. Krutyanskiy, M. Meraner, J. Schupp, V. Krcmarsky, H. Hainzer, B. P. Lanyon, *npj Quantum Inf.* **2019**, 5, 72.

[6] W. K. Wootters, W. H. Zurek, *Nature* **1982**, 299, 802.

[7] H.-J. Briegel, W. Dür, J. I. Cirac, P. Zoller, *Phys. Rev. Lett.* **1998**, 81, 26.

[8] E. M. Purcell, in *Proceedings of the American Physical Society*, vol. 69, American Physical Society (APS), **1946**, p. 674.

[9] A. E. Rugar, S. Aghaeimeibodi, D. Riedel, C. Dory, H. Lu, P. J. McQuade, Z.-X. Shen, N. A. Melosh, J. Vučković, *Phys. Rev. X* **2021**, 11, 031021.

[10] K. Kuruma, B. Pingault, C. Chia, D. Renaud, P. Hoffmann, S. Iwamoto, C. Ronning, M. Lončar, *Appl. Phys. Lett.* **2021**, 118, 230601.

[11] E. N. Knall, C. M. Knaut, R. Bekenstein, D. R. Assumpcao, P. L. Stroganov, W. Gong, Y. Q. Huan, P.-J. Stas, B. Machielse, M. Chalupnik, D. Levonian, A. Suleymanzade, R. Riedinger, H. Park, M. Lončar, M. K. Bhaskar, M. D. Lukin, *Phys. Rev. Lett.* **2022**, 129, 053603.

[12] S. Mouradian, N. H. Wan, T. Schröder, D. Englund, *Appl. Phys. Lett.* **2017**, 111, 021103.

[13] R. E. Evans, M. K. Bhaskar, D. D. Sukachev, C. T. Nguyen, A. Sipahigil, M. J. Burek, B. Machielse, G. H. Zhang, A. S. Zibrov, E. Bielejec, H. Park, M. Lončar, M. D. Lukin, *Science* **2018**, 362, 6415.

[14] J. E. Fröch, S. Kim, C. Stewart, X. Xu, Z. Du, M. Lockrey, M. Toth, I. Aharonovich, *Nano Lett.* **2020**, 20, 2784.

[15] A. Goban, C.-L. Hung, S.-P. Yu, J. D. Hood, J. A. Muniz, J. H. Lee, M. J. Martin, A. C. McClung, K. S. Choi, D. E. Chang, O. Painter, H. J. Kimble, *Nat. Commun.* **2014**, 5, 3808.

[16] Y. Akahane, T. Asano, B.-S. Song, S. Noda, *Nature* **2003**, 425, 944.

[17] Q. Quan, P. B. Deotare, M. Loncar, *Appl. Phys. Lett.* **2010**, 96, 203102.

[18] M. J. Burek, C. Meuwly, R. E. Evans, M. K. Bhaskar, A. Sipahigil, S. Meesala, B. Machielse, D. D. Sukachev, C. T. Nguyen, J. L. Pacheco, E. Bielejec, M. D. Lukin, M. Lončar, *Phys. Rev. Appl.* **2017**, 8, 024026.

[19] M. Palamaru, P. Lalanne, *Appl. Phys. Lett.* **2001**, 78, 1466.

[20] C. Sauvan, G. Lecamp, P. Lalanne, J. P. Hugonin, *Opt. Express* **2005**, 13, 245.

[21] A. Reiserer, G. Rempe, *Rev. Modern Phys.* **2015**, 87, 1379.

[22] N. Tomm, A. Javadi, N. O. Antoniadis, D. Najer, M. C. Löbl, A. R. Korsch, R. Schott, S. R. Valentin, A. D. Wieck, A. Ludwig, R. J. Warburton, *Nat. Nanotechnol.* **2021**, 16, 399.

[23] L. Li, T. Schröder, E. H. Chen, M. Walsh, I. Bayn, J. Goldstein, O. Gaathon, M. E. Trusheim, M. Lu, J. Mower, M. Cotlet, M. L. Markham, D. J. Twitchen, D. Englund, *Nat. Commun.* **2015**, 6, 6173.

[24] T. Gaebel, I. Popa, A. Gruber, M. Domhan, F. Jelezko, J. Wrachtrup, *New J. Phys.* **2004**, 6, 98.

[25] T. Iwasaki, Y. Miyamoto, T. Taniguchi, P. Siyushev, M. H. Metsch, F. Jelezko, M. Hatano, *Phys. Rev. Lett.* **2017**, 119, 253601.

[26] J. Görlitz, D. Herrmann, P. Fuchs, T. Iwasaki, T. Taniguchi, D. Rogalla, D. Hardeman, P.-O. Colard, M. Markham, M. Hatano, C. Becher, *npj Quantum Inf.* **2022**, 8, 45.

[27] M. W. Doherty, N. B. Manson, P. Delaney, F. Jelezko, J. Wrachtrup, L. C. L. Hollenberg, *Phys. Rep.* **2013**, 528, 1.

[28] C. Bradac, W. Gao, J. Forneris, M. E. Trusheim, I. Aharonovich, *Nat. Commun.* **2019**, 10, 5625.

[29] H. R. Phillip, E. A. Taft, *Phys. Rev.* **1964**, 136, A1445.

[30] S. Chakravarthi, C. Pederson, Z. Kazi, A. Ivanov, K.-M. C. Fu, *Phys. Rev. B* **2021**, 104, 085425.

[31] L. Orphal-Kobin, K. Unterguggenberger, T. Pregnolato, N. Kemf, M. Matalla, R.-S. Unger, I. Ostermay, G. Pieplow, T. Schröder, *Phys. Rev. X* **2022**, 13, 011042.

[32] S. Y. Lin, G. Arjavalingam, *J. Opt. Soc. Am. B* **1994**, 11, 10.

[33] I. Bayn, S. Mouradian, L. Li, J. A. Goldstein, T. Schröder, J. Zheng, E. H. Chen, O. Gaathon, M. Lu, A. Stein, C. A. Ruggiero, J. Salzman, R. Kalish, D. Englund, *Appl. Phys. Lett.* **2014**, 105, 211101.

[34] J. Močkus, in *Optimization techniques IFIP technical conference*, Springer, Berlin, Heidelberg **1975**, p. 400.

[35] J. Gallego, W. Alt, T. Macha, M. Martinez-Dorantes, D. Pandey, D. Meschede, *Phys. Rev. Lett.* **2018**, 121, 173603.

[36] C. Hepp, T. Müller, V. Waselowski, J. N. Becker, B. Pingault, H. Sternschulte, D. Steinmüller-Nethl, A. Gali, J. R. Maze, M. Atatüre, C. Becher, *Phys. Rev. Lett.* **2014**, 112, 036405.

[37] J. Görlitz, D. Herrmann, G. Thiering, P. Fuchs, M. Gandil, T. Iwasaki, T. Taniguchi, M. Kieschnick, J. Meijer, M. Hatano, A. Gali, C. Becher, *New J. Phys.* **2020**, 22, 013048.

[38] T. G. Tiecke, K. P. Nayak, J. D. Thompson, T. Peyronel, N. P. de Leon, V. Vuletić, M. D. Lukin, *Optica* **2015**, 2, 2.

[39] A. G. Fowler, D. S. Wang, C. D. Hill, T. D. Ladd, R. V. Meter, L. C. L. Hollenberg, *Phys. Rev. Lett.* **2010**, 104, 180503.

[40] W. J. Munro, A. M. Stephens, S. J. Devitt, K. A. Harrison, K. Nemoto, *Nat. Photonics* **2012**, 6, 777.

[41] S. Muralidharan, J. Kim, N. Lütkenhaus, M. D. Lukin, L. Jiang, *Phys. Rev. Lett.* **2014**, 112, 250501.

[42] K. Azuma, K. Tamaki, H.-K. Lo, *Nat. Commun.* **2015**, 6, 6787.

[43] A. N. Glaudell, E. Waks, J. M. Taylor, *New J. Phys.* **2016**, 18, 093008.

[44] F. Ewert, M. Bergmann, P. van Loock, *Phys. Rev. Lett.* **2016**, 117, 210501.

[45] S.-W. Lee, T. C. Ralph, H. Jeong, *Phys. Rev. A* **2019**, 100, 052303.

[46] V. Scarani, H. Bechmann-Pasquinucci, N. J. Cerf, M. Dušek, N. Lütkenhaus, M. Peev, *Rev. Modern Phys.* **2009**, 81, 1301.

[47] J. D. Joannopoulos, S. G. Johnson, J. N. Winn, R. D. Meade, *Photonic Crystals*, 2nd edition, Princeton University Press, Princeton, USA, **2008**.

[48] P. Tamarat, T. Gaebel, J. R. Rabeau, M. Khan, A. D. Greentree, H. Wilson, L. C. L. Hollenberg, S. Prawer, P. Hemmer, F. Jelezko, J. Wrachtrup, *Phys. Rev. Lett.* **2006**, 97, 083002.

[49] L. J. Rogers, K. D. Jahnke, T. Teraji, L. Marseglia, C. Müller, B. Naydenov, H. Schauffert, C. Kranz, J. Isoya, L. P. McGuinness, F. Jelezko, *Nat. Commun.* **2014**, 5, 4739.

[50] P. Siyushev, M. H. Metsch, A. Ijaz, J. M. Binder, M. K. Bhaskar, D. D. Sukachev, A. Sipahigil, R. E. Evans, C. T. Nguyen, M. D. Lukin, P. R. Hemmer, Y. N. Palyanov, I. N. Kupriyanov, Y. M. Borzdov, L. J. Rogers, F. Jelezko, *Phys. Rev. B* **2017**, 96, 081201(R).

[51] M. E. Trusheim, B. Pingault, N. H. Wan, M. Gündoğan, L. D. Santis, R. Debroux, D. Gangloff, C. Purser, K. C. Chen, M. Walsh, J. J. Rose, J. N. Becker, B. Lienhard, E. Bersin, I. Paradeisanos, G. Wang, D. Lyzwa, A. R.-P. Montblanch, G. Malladi, H. Bakhru, A. C. Ferrari, I. A. Walmsley, M. Atatüre, D. Englund, *Phys. Rev. Lett.* **2020**, 124, 023602.

[52] C. Santori, P. E. Barclay, K.-M. C. Fu, R. G. Beausoleil, S. Spillane, M. Fisch, *Nanotechnology* **2010**, 21, 274008.

[53] E. Neu, D. Steinmetz, J. Riedrich-Möller, S. Gsell, M. Fischer, M. Schreck, C. Becher, *New J. Phys.* **2011**, *13*, 025012.

[54] Y. N. Palyanov, I. N. Kupriyanov, Y. M. Borzdov, N. V. Surovtsev, *Sci. Rep.* **2015**, *5*, 14789.

[55] M. K. Bhaskar, R. Riedinger, B. Machielse, D. S. Levonian, C. T. Nguyen, E. N. Knall, H. Park, D. Englund, M. Lončar, D. D. Sukachev, M. D. Lukin, *Nature* **2020**, *580*, 60.

[56] J. Chang, J. W. N. Los, J. O. Tenorio-Pearl, N. Noordzij, R. Gourgues, A. Guardiani, J. R. Zichi, S. F. Pereira, H. P. Urbach, V. Zwiller, S. N. Dorenbos, I. E. Zadeh, *APL Photonics* **2021**, *6*, 036114.

[57] JCMsuite (Simulation Suite for Nano-Optics), JCMwave GmbH, Bolivarallee 22, 14050 Berlin, Germany.

[58] P.-I. Schneider, X. Garcia Santiago, V. Soltwisch, M. Hammerschmidt, S. Burger, C. Rockstuhl, *ACS Photonics* **2019**, *6*, 11.